DOI: 10.1002/ejic.200901158

Synthesis, Structures, and Magnetic Properties of *N*-Trialkylsilyl-8-amidoquinoline Complexes of Chromium, Manganese, Iron, and Cobalt as well as of Wheel-Like Hexanuclear Iron(II) and Manganese(II) Bis(8-amidoquinoline)

Astrid Malassa,[a] Christine Agthe,[a] Helmar Görls,[a] Maren Podewitz,[b] Lian Yu,[b] Carmen Herrmann,[b] Markus Reiher,*[b] and Matthias Westerhausen*[a]

Keywords: Amides / Wheel structures / Chromium / Manganese / Cobalt / Iron / Magnetic properties

The transamination of 8-(*tert*-butyldimethylsilylamino)quinoline with $(thf)_2Cr[N(SiMe_3)_2]_2$ yields monomeric bis[8-(*tert*-butyldimethylsilylamido)quinoline]chromium(II) (**1**). Similar reactions of $M[N(SiMe_3)_2]_2$ (M = Mn, Fe, Co) with 8-(trialkylsilylamino)quinoline lead to the formation of monomeric bis[8-(trialkylsilylamido)quinoline]metal(II) [M = Mn, SiR_3 = $SiMe_2tBu$ (**2a**), $SiiPr_3$ (**2b**); M = Fe, SiR_3 = $SiMe_2tBu$ (**3a**), $SiiPr_3$ (**3b**); M = Co, SiR_3 = $SiMe_2tBu$ (**4a**), $SiiPr_3$ (**4b**)]. The transamination of 8-aminoquinoline with $M[N(SiMe_3)_2]_2$ (M = Mn, Fe, Co) allows the isolation of the heteroleptic 1:1 and homoleptic 2:1 products. The 1:1 complexes bis[8-amidoquinoline metal(II)bis(trimethylsilyl)amide] [M = Mn (**5**), Fe (**6**), Co (**7**)] are dimeric with bridging 8-amidoquinoline moieties. The 2:1 complexes of Mn and Fe, bis(8-amidoquinoline)manganese(II) (**8**) and bis(8-amidoquinoline)iron(II) (**9**), form hexamers with wheel-like molecular structures consisting of metal-centered nitrogen octahedra interconnected by common N···N edges. The cobalt complex, bis(8-amidoquinoline)cobalt(II) (**10**), precipitates as a microcrystalline powder. Investigations of the magnetic properties by DFT corroborate the experimental data for the Mn derivative **8**, where an antiferomagnetic coupling is observed. By contrast, calculations on the Fe_6-wheel **9** yield very close-lying ferromagnetically and antiferromagnetically coupled states.

Introduction

N-Trialkylsilyl-substituted 2-pyridylmethylamido ligands form monomeric complexes with the late divalent 3d transition metals. The molecular structures are very similar for Mg^{2+}, Mn^{2+}, Fe^{2+}, Co^{2+}, and Zn^{2+} and depend solely on the radius of the metal atom.[1] The related 8-(trialkylsilylamido)quinoline complexes of Mg^{2+}, Zn^{2+}, and Ni^{2+} show similar molecular structures.[2,3] In all of these molecules, the metal cations M^{2+} are in distorted tetrahedral environments. This behavior can be explained by the assumption that the bulkiness of the trialkylsilyl groups only allows an arrangement of the ligands as observed because of repulsive steric forces. This conclusion is supported by the observation that unsubstituted 8-amidoquinoline complexes of Zn^{2+} show a distorted tetrahedral coordination sphere, whereas Ni^{2+} has a square-planar environment, which is characteristic for a low-spin d^8 system.[4] In contrast to the complexes of the late 3d transition metals with neutral 8-quinoline ligands,[5] there are nearly no investigations on compounds with anionic 8-amidoquinoline groups.

It was observed earlier that the late transition metals show a reluctance to form stable amides.[6] Therefore, oligonuclear wheel-shaped complexes of Fe^{III} (ferric wheels) and Fe^{II} (ferrous wheels) employ multidentate oxygen bases.[7] A large variety of ferric wheels is known,[8] and intense quantum chemical studies[9] in order to understand the magnetic properties were undertaken. However, only a rather limited number of reports on ferrous wheels have been published as of yet. Compounds of the type $[M(\mu\text{-}X)(\mu\text{-}SSitBu_3)]_{12}$ with M = Fe, Co, Ni and X = Cl, Br, I show the formation of wheel-like molecules.[10] Isoelectronic to Fe^{III}, Mn^{II} often is also used in order to prepare high-nuclearity, high-spin, wheel-shaped molecules employing ligands with oxygen donor atoms.[11] Oligonuclear amido and/or imido complexes of Mn^{II} often form cage compounds rather than wheel-shaped molecules.[12] Because of the fact that high-spin Mn^{II} exhibits the maximum number of unpaired electrons, often large spin states are accessible even though the maximum number of unpaired electrons is not always realized.[13]

On the basis of our investigations on 2-pyridylmethylamides[1] and related 8-amidoquinolines,[4] we were interested in the structure–property relationship with respect to

---

[a] Institut für Anorganische und Analytische Chemie, Friedrich-Schiller-Universität Jena,
August-Bebel-Str. 2, 07743 Jena, Germany
Fax: +49-3641-948110
E-mail: m.we@uni-jena.de
[b] Laboratorium für Physikalische Chemie, ETH Zürich,
Hönggerberg Campus, Wolfgang-Pauli-Str. 10, 8093 Zürich, Switzerland
Fax: +41-44-63-31594
E-mail: markus.reiher@ phys.chem.ethz.ch

the radius of M^{2+} and the nature of the metal. Transition-metal-mediated CH activation of 2-pyridylmethyl moieties was observed earlier. Recent examples include the oxidative dehydrogenation of 2-pyridylmethylamines at iron[14] or cobalt[15,16] as well as of 2-pyridylmethylphosphanes.[17–19] Even dimethylzinc is able to oxidize shielded (2-pyridylmethyl)(trialkylsilyl)amides to yield 1,2-bis(2-pyridyl)-1,2-bis(trialkylsilylamido)bis(methylzinc) according to Equation (1).[20,21] These side reactions can be avoided by employing the related 8-aminoquinoline, which allows the investigation of the coordination behavior of these ligands. In addition, it can be expected that its deprotonated form, the 8-amidoquinoline ligand, also forms stable complexes with the late transition metals.

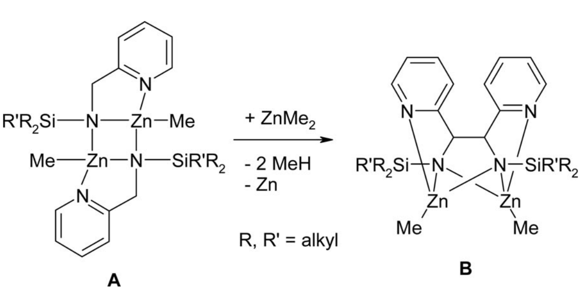

(1)

Polynuclear transition-metal clusters often exhibit magnetically coupled metal centers but because of the complicated molecular structure, the interpretation of the experimental data may not always be unambiguous. Quantum chemical calculations of the different spin states and the local spin distributions[22,23] are therefore necessary to shed some light on potential spin–spin couplings.[24]

Results and Discussion

Syntheses

The transamination of manganese(II), iron(II), and cobalt(II) bis[bis(trimethylsilyl)amide] with 8-(trialkylsilylamino)quinoline yielded bis[8-(trialkylsilylamido)quinoline]manganese(II) (**2**), -iron(II) (**3**), and -cobalt(II) (**4**), respectively, according to Equation (2). Intermediates such as the heteroleptic mono-transamination products were not observed. An equimolar stoichiometry of the starting materials left half of the metal component unreacted in the reaction mixture. Contrary to these observations, the metallation reaction of *N*-trialkylsilyl-8-amidoquinoline with $Zn[N(SiMe_3)_2]_2$ in a molar 1:1 ratio gave the heteroleptic derivative with a three-coordinate zinc atom.[4] Deprotonation of 8-(*tert*-butyldimethylsilylamido)quinoline with distorted square-planar $(thf)_2Cr[N(SiMe_3)_2]_2$ yielded bis[8-(trialkylsilylamido)quinoline]chromium(II) (**1**). Similar structures were also found for the corresponding magnesium(II),[2] zinc(II)[2] and nickel(II) complexes.[3]

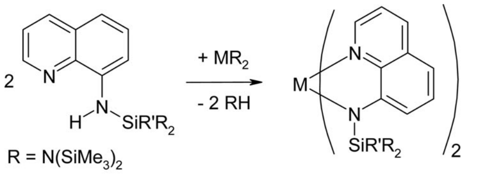

R	R'	Cr	Mn	Fe	Co
Me	*t*Bu	**1**	**2a**	**3a**	**4a**
*i*Pr	*i*Pr		**2b**	**3b**	**4b**

(2)

The metallation of 8-aminoquinoline with $M[N(SiMe_3)_2]_2$ (M = Mn, Fe, and Co) gave heteroleptic dimeric 8-amidoquinoline metal-bis(trimethylsilyl)amide [Mn (**5**), Fe (**6**) and Co (**7**), Equation (3)], which crystallize isomorphously. The molecules are dimeric with the 8-amidoquinoline groups in bridging positions. The basicity of the trialkylsilyl-substituted amides is strongly reduced because of an effective negative hyperconjugation and charge back-donation from the $p_z(N)$ lone pair into σ*(Si–C) orbital of the trialkylsilyl groups. Because of this fact, trialkylsilyl-substituted amido groups avoid bridging positions, which explains the observation that sterically shielded homoleptic trialkylsilyl-substituted 8-amidoquinolines are favored over heteroleptic compounds with three-coordinate metal atoms.

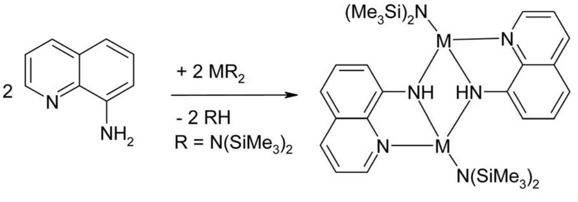

M = Mn (**5**), Fe (**6**), Co (**7**) (3)

A 2:1 stoichiometry of 8-aminoquinoline and $M[N(SiMe_3)_2]_2$ (M = Mn, Fe, Co), respectively, in the transamination reactions yielded the expected bis(8-amidoquinoline)metal(II) complexes of manganese (**8**), iron (**9**) [Equation (4)], and cobalt (**10**) [Equation (5)]. The molecular structures of **8** and **9** were confirmed by X-ray structural investigations and show the crystallization of hexanuclear wheel-shaped molecules, referred to as [M_6], whereas the

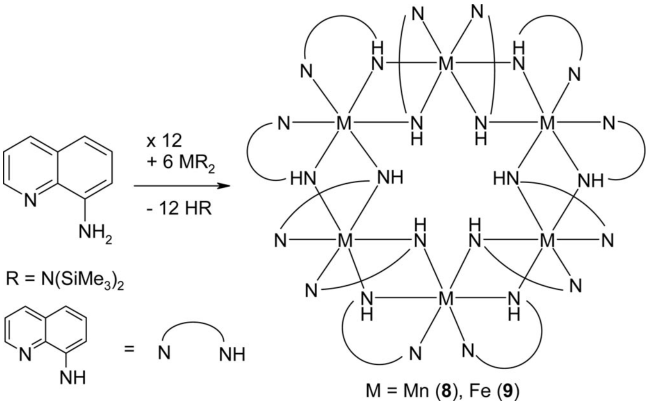

M = Mn (**8**), Fe (**9**)

(4)

crystals of **10** were not suitable for an X-ray structure determination and neither aggregation degree nor coordination number of the cobalt atom are known.

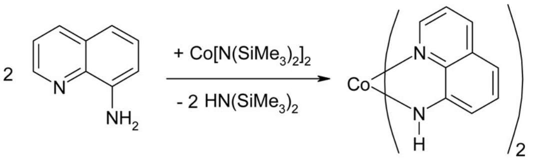

10

(5)

Molecular Structures

The molecular structures of the bis[8-(trialkylsilylamido)quinoline] complexes of chromium(II) (**1**), manganese(II) (**2**), iron(II) (**3**), and cobalt(II) (**4**) are summarized in Table 1 for those that contain a crystallographic C_2 axis (monoclinic space groups) and in Table 2 for those without this symmetry element (triclinic space groups). The molecular structures and numbering schemes of representative examples **1**, **3a**, and **3b** are shown in Figures 1, 2, and 3, respectively. The triisopropylsilyl group induces larger steric strain than the *tert*-butyldimethylsilyl substituents. The size of the bulky trialkylsilyl group has almost no influence on the 8-(trialkylsilylamido)quinoline ligand: (i) the N–Si bond lengths lie between 172.7(2) and 174.9(2) pm; (ii) the C–N–Si bond angles vary between 121.3(2)° and 127.1(2)°; (iii) the bite angle is also indicative of the metal size – the intraligand N–M–N angle decreases with increasing metal radius.

The M–N distances increase with increasing radii of the metal cations. The chromium derivative **1** represents an exception, with short Cr–N bonds for a rather large radius of the Cr^{2+} cation. The properties and reactivity of starting $(thf)_2Cr[N(SiMe_3)_2]_2$ also deviate strongly from those of the derivatives of the later 3d transition metals. This chromium derivative contains a metal atom in a distorted square-planar environment with Cr–N bond lengths of 209(1) pm.[25] This compound can easily be oxidized by iodine to yield $[(Me_3Si)_2N]_2CrI_2$ with a tetrahedral Cr^{IV} center with Cr–N distances of 183.6(1) pm.[26] The manganese(II) complex $(thf)_2Mn[N(SiMe_3)_2]_2$ exhibits a tetrahedral environment around the metal center with Mn–N bond lengths of 203.3(5) and 204.8(5) pm.[27] The iron complex crystallizes as the mono(thf) complex $(thf)Fe[N(SiMe_3)_2]_2$ with Fe–N values of 191.6(5) pm with a distorted trigonal-planar iron atom.[28] Whereas solvent-free $M[N(SiMe_3)_2]_2$ with M = Mn, Fe, Co is monomeric in the gaseous phase[29] and dimeric in the solid state,[28,30,31] there are no reports on the structure of the corresponding Cr derivative. In contrast to the short Cr–N bonds of **1**, the manganese derivatives **2a** (Table 1) and **2b** (Table 2) show longer Mn–N distances than expected with respect to the radius of the Mn^{2+} cation. The superposition of the molecules of **1** and **3a** is shown in Figure 4.

Table 1. Selected structural data of bis[8-(trialkylsilylamido)quinoline]metal(II) complexes (bond lengths [Å], bond angles [°]) that crystallize in the monoclinic space group and display the same numbering scheme.

	Cr (**1**)	Mn (**2a**)	Fe (**3a**)	Co (**4b**)	
$r(M^{2+})$ [pm]	87	80	77	72	
$r(M_{metal})$ [pm]	129	137	126	125	
SiR''_2	$SiMe_2tBu$	$SiMe_2tBu$	$SiMe_2tBu$	$SiiPr_3$	
Molecule				A	B
M–N1	207.2(2)	215.9(2)	209.3(2)	204.1(2)	204.1(2)
M–N2	205.3(2)	206.1(2)	199.8(2)	198.1(2)	196.7(2)
N2–M–N2A	162.5(2)	160.52(9)	160.2(1)	133.24(9)	133.38(9)
N2–M–N1	80.91(9)	80.32(6)	82.39(7)	83.96(7)	84.52(7)
N2–M–N1A	106.10(9)	111.18(6)	109.22(8)	123.28(7)	122.63(7)
N1–M–N1A	133.9(1)	110.41(8)	110.2(1)	112.06(9)	111.79(9)
Si–N2	173.2(3)	172.7(2)	173.0(2)	174.0(2)	174.4(2)
Si–N2–M	121.9(1)	119.63(8)	120.5(1)	125.1(1)	126.7(1)
C8–N2–Si	125.4(2)	127.1(1)	126.8(2)	124.1(2)	122.4(1)
C8–N2–M	112.1(2)	113.1(1)	112.6(2)	110.1(1)	110.0(1)
N1–C1	132.7(4)	132.2(3)	132.0(3)	132.5(3)	132.7(3)
N1–C9	137.3(4)	136.8(2)	137.5(3)	136.9(3)	136.8(3)
N2–C8	137.4(4)	137.6(2)	138.4(3)	137.5(3)	138.2(3)
C1–C2	139.8(4)	140.1(3)	140.2(4)	139.8(3)	139.3(3)
C2–C3	136.1(5)	136.0(3)	135.7(4)	127.4(3)	136.9(3)
C3–C4	141.0(5)	141.4(3)	141.1(4)	140.8(3)	141.6(3)
C4–C5	141.2(5)	140.6(3)	141.3(4)	140.6(3)	141.1(3)
C4–C9	141.5(4)	142.3(3)	140.8(3)	142.4(3)	141.9(3)
C5–C6	136.1(5)	136.3(3)	136.5(4)	136.7(3)	136.5(3)
C6–C7	140.6(5)	140.5(3)	140.1(4)	139.9(3)	140.5(3)
C7–C8	140.1(4)	139.9(3)	139.1(3)	140.1(3)	139.6(3)
C8–C9	143.9(4)	144.8(3)	144.6(3)	144.7(3)	144.7(3)

Table 2. Selected structural data of bis[8-(trialkylsilylamido)quinoline]metal(II) complexes (bond lengths [Å], bond angles [°]) that crystallize in the triclinic space group $P\bar{1}$ and display the same numbering scheme.

	Mn (**2b**)		Fe (**3b**)		Ni[3b]	
$r(M^{2+})$ [pm]	80		77		69	
$r(M_{metal})$ [pm]	137		126		124	
SiR''_2	$SiiPr_3$		$SiiPr_3$		$SiiPr_3$	
Molecule	A	B	A	B	A	B
M–N1	216.1(3)	215.8(3)	209.2(3)	209.6(2)	200.2(2)	200.5(2)
M–N2	207.6(3)	205.8(3)	200.6(2)	199.6(3)	197.7(2)	196.2(2)
N2–M–N1	81.1(1)	81.0(1)	83.2(1)	82.9(1)	84.11(8)	83.97(8)
M–N3	217.1(3)	216.7(3)	209.7(3)	209.5(3)	200.1(2)	200.3(2)
M–N4	206.3(3)	206.7(3)	199.9(2)	200.5(2)	195.5(2)	196.0(2)
N4–M–N3	80.9(1)	80.8(1)	82.8(1)	82.6(1)	84.63(9)	84.298(9)
N2–M–N4	149.2(1)	149.6(1)	150.3(1)	151.1(1)	148.43(9)	148.84(9)
N2–M–N3	111.9(1)	114.8(1)	110.00(9)	112.5(1)	109.19(9)	112.36(9)
N1–M–N3	98.3(1)	106.2(1)	96.7(1)	103.8(1)	98.12(9)	103.12(9)
Si1–N2	173.8(3)	173.8(3)	174.7(3)	174.1(3)	175.4(2)	174.4(2)
Si1–N2–M	121.8(1)	123.2(1)	122.0(0)	123.5(1)	122.9(1)	124.1(1)
C8–N2–Si1	126.3(2)	124.2(2)	126.1(2)	124.4(2)	125.4(2)	124.0(2)
C8–N2–M	111.4(2)	112.5(2)	111.5(2)	112.0(2)	111.3(2)	111.8(2)
Si2–N4	173.6(3)	173.5(3)	174.9(2)	174.0(3)	175.5(2)	174.5(2)
Si2–N4–M	126.3(2)	122.1(1)	127.3(1)	122.4(1)	128.4(1)	123.5(1)
C17–N4–Si2	122.1(2)	125.6(2)	121.3(2)	125.8(2)	120.9(2)	125.0(2)
C17–N4–M	111.5(2)	112.2(2)	111.4(2)	111.7(2)	110.7(2)	111.4(2)

The size of the trialkylsilyl groups strongly influences the N–M–N angles between the amido nitrogen atoms N2 and N4; larger values of more than 160° are found for the deriv-

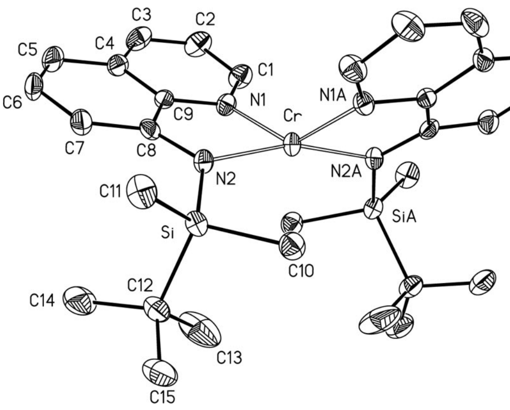

Figure 1. Molecular structure and numbering scheme of **1**. The ellipsoids are drawn at the 40% probability level. H atoms are omitted for clarity. Symmetry-related atoms (–*x*, *y*, –*z* + 0.5) are marked with an “A”.

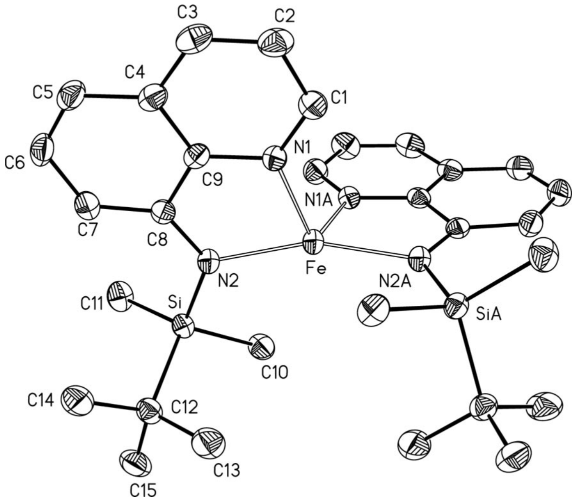

Figure 2. Molecular structure and numbering scheme of **3a**. The ellipsoids are drawn at the 40% probability level. H Atoms are omitted for clarity. Symmetry-related atoms (–*x*, *y*, –*z* + 0.5) are marked with “A”.

atives **1**, **2a**, and **3a** with $SiMe_2tBu$ substituents. The larger $SiiPr_3$ groups lead to smaller values of approximately 150°. The cobalt derivative **3b** (R = $SiiPr_3$) exhibits very small N2–Co–N2′ bond angles of 133.3° (Tables 1 and 2). The superposition of the molecules of **3b** and **4b** is shown in Figure 5.

The molecular structure and numbering scheme of **6** are shown in Figure 6. This complex represents a characteristic example of this compound class of the type $[(Me_3Si)_2N–M\{\mu\text{-}N(H)C_9NH_6\}]_2$ with M = Mn, Fe, and Co [$N(H)C_9NH_6$ represents the 8-amidoquinoline ligand]. Structural parameters are listed in Table 3. The corresponding chromium complex was not accessible by this preparative procedure. For comparison reasons, the already-known Zn derivative[4] is included. In this row, the trend in the M–N bond lengths follows the variation of the metal radii. The smallest M–N bond lengths are observed for the terminally bound bis(trimethylsilyl)amido group, because N3 has the low coordination number of 3 and electrostatic attraction between the $(Me_3Si)_2N$ anion and the metal cation also leads to a shortening of this bond. The anionic charge at

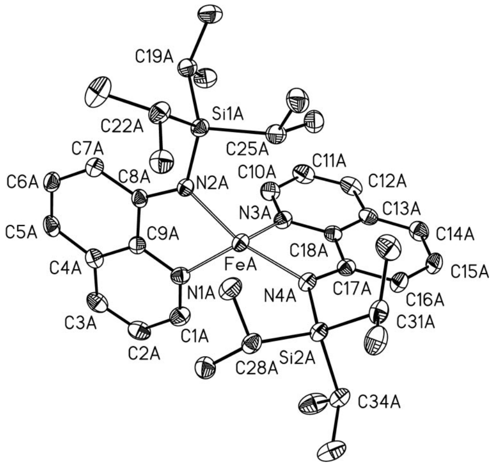

Figure 3. Molecular structure and numbering scheme of molecule A of **3b**. The ellipsoids are drawn at the 40% probability level. H Atoms are omitted for clarity. The letters “A” and “B” are chosen in order to distinguish between molecule A and molecule B (not shown here).

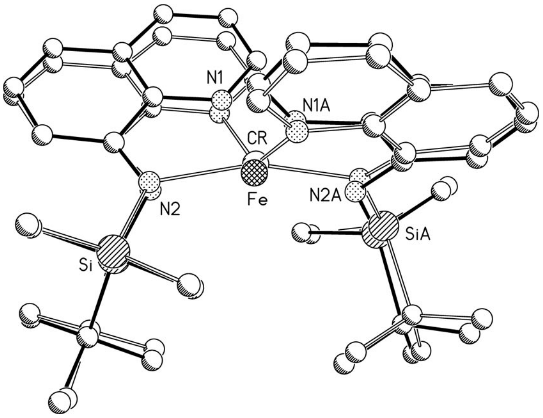

Figure 4. Superposition of the molecules of **1** and **3a**. The atoms are drawn with arbitrary radii.

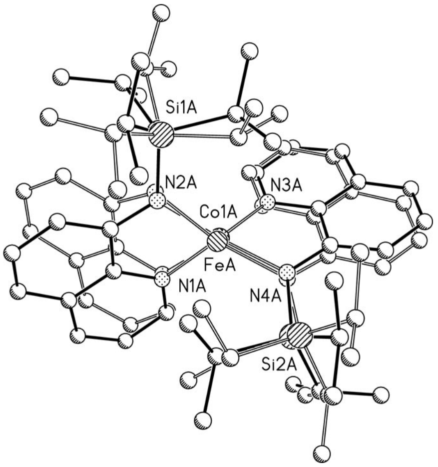

Figure 5. Superposition of the molecules of **3b** and **4b**. The atoms are shown with arbitrary radii.

N2 is delocalized within the quinoline π-system, which leads to a shortening of the N2–C8 bond relative to that of free 8-aminoquinoline.[32]

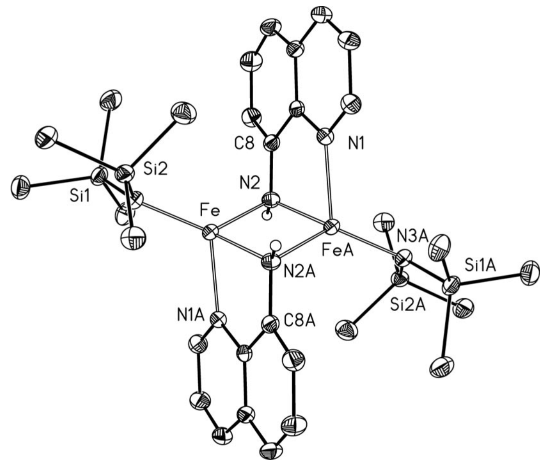

Figure 6. Molecular structure of **6**. The ellipsoids are drawn at the 40% probability level. The hydrogen atoms, with the exception of those of the amide groups, are omitted for clarity. Symmetry-equivalent atoms ($-x+2$, $-y+1$, $-z+1$) are marked with "A".

Table 3. Comparison of selected bond lengths [pm] and angles [°] of heteroleptic bis(trimethylsilyl)amidometal(II) 8-amidoquinolines of manganese (**5**), iron (**6**), cobalt (**7**), and zinc. Symmetry-related atoms are marked with a prime.

M	Mn (**5**)	Fe (**6**)	Co (**7**)	Zn[4]
$r(M^{2+})$ [pm]	80	77	72	74
M–N1	220.3(2)	214.5(2)	207.7(3)	210.8(2)
M–N2	213.9(2)	210.0(2)	203.6(3)	206.3(2)
M–N2′	217.7(2)	208.6(2)	204.5(3)	208.9(2)
M–N3	201.3(2)	194.9(2)	193.8(3)	192.1(2)
N3–Si1	171.7(2)	171.2(2)	171.6(3)	171.9(2)
N3–Si2	170.7(2)	172.4(2)	171.4(3)	171.3(2)
N2–C8	140.1(3)	140.3(3)	139.3(5)	139.7(3)
N1–C1	132.4(3)	132.1(3)	133.0(5)	132.4(3)
N1–C9	137.9(3)	137.4(3)	137.0(5)	137.7(3)
M···M	295.17(9)	284.28(6)	271.6(1)	286.98(4)
M–N3–Si1	113.8(1)	115.98(9)	113.4(2)	113.08(9)
M–N3–Si2	115.7(1)	113.81(9)	117.3(2)	117.0(1)
Si1–N3–Si2	125.7(1)	125.0(1)	124.9(2)	125.0(1)
N2–M–N2′	93.72(9)	94.44(6)	96.5(1)	92.56(7)

A strong dependency between the nature of the metal and the molecular structure is observed for the bis(8-amidoquinoline)metal complexes. Whereas a monomeric compound with a distorted tetrahedrally coordinated metal atom is observed for M = Zn,[4] hexameric molecules form for M = Mn and Fe. In these molecules, the metal atoms are embedded in distorted octahedrons of nitrogen atoms. These octahedrons are connected by common N···N edges, and the hexanuclear molecule forms a wheel-like structure as shown in Figure 7. The different molecular structures for the late 3d metals (Mn, Fe: wheel-like, MN_6 octahedrons; Zn: monomeric, MN_4 tetrahedrons; Ni: monomeric, square planar) depend on the size of the metals: Mn^{2+} and Fe^{2+} are large enough for octahedral environments whereas Zn^{2+} prefers tetrahedral coordination spheres. For Ni^{2+}, ligand-field splitting leads to square-planar coordination spheres. In contrast to low-spin Co and Ni complexes, the wheel-shaped molecules contain high-spin manganese(II) and iron(II). However, in the Fe compound a ferromagnetic coupling is observed whereas the Mn derivative shows an antiferromagnetic coupling.

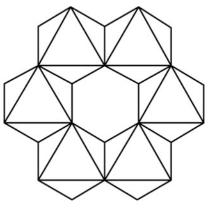

Figure 7. Connectivity of the MN_6 octahedrons.

The molecular structure of [Fe_6] (**9**) is shown in Figure 8. The manganese complex [Mn_6] (**8**) crystallizes isotypically. The metal atoms are in distorted octahedral environments

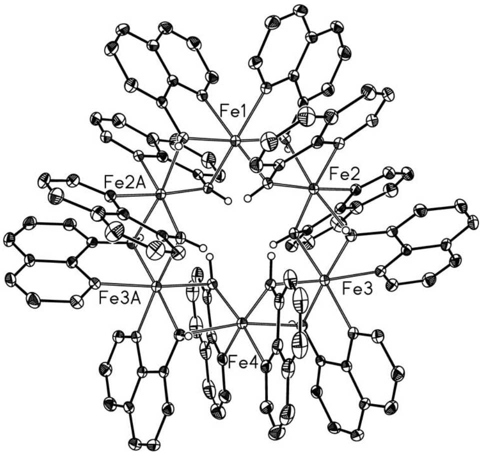

Figure 8. Molecular structure of **9**. The ellipsoids are drawn at the 40% probability level. The hydrogen atoms, with the exception of those of the amide moieties, are neglected for clarity. Symmetry-related iron atoms ($-x$, y, $-z+0.5$) are marked with "A". The Mn^{II} complex **8** crystallizes isotypically.

Table 4. Selected bond lengths [pm] and angles [°] of the isotypic wheel-like molecules [Mn_6] (**8**) and [Fe_6] (**9**). The different 8-amidoquinoline groups are distinguished by the letters A, B, C, D, E, and F; symmetry-related atoms are marked with a prime.

	[Mn_6] (**8**)	[Fe_6] (**9**)
M1–N1A	227.3(7)	219.5(3)
M1–N2A	216.6(7)	209.9(3)
M1–N2B	231.0(7)	228.4(3)
M2–N2A′	237.7(7)	229.8(3)
M2–N1B	228.8(7)	224.1(3)
M2–N2B	218.7(6)	212.5(3)
M2–N1C	230.9(6)	227.8(3)
M2–N2C	217.7(7)	211.9(3)
M2–N2D	234.9(7)	228.7(3)
M3–N2C	234.2(6)	229.8(3)
M3–N1D	228.3(6)	219.8(3)
M3–N2D	216.1(7)	209.4(3)
M3–N1E	225.6(6)	219.0(3)
M3–N2E	213.5(7)	208.9(3)
M3–N2F′	234.5(6)	231.1(3)
M4–N2E	245.0(6)	239.5(3)
M4–N1F	227.4(7)	224.0(3)
M4–N2F	213.6(7)	210.0(3)

in which the amido fragments are in bridging positions and the pyridyl moieties are bound terminally. Therefore, all metal atoms are coordinated by four amido ligands and two pyridyl groups arranged in a *cis* manner. The octahedrons, which are metal-centered, are interconnected by common edges. This leads to large M···M contacts of more than 300 pm. Because the metal atoms have a coordination number of six, large Mn–N and Fe–N distances of 213.5(7)–245.0(6) and 209.4(3)–239.5(3) pm, respectively, are observed. Table 4 contains selected structural data of these wheel-like coordination compounds.

Magnetic Properties

The molecular structures of hexanuclear wheel-like [Mn_6] and [Fe_6] are very similar, but the magnetic behaviors differ significantly. In contrast to the manganese derivative **8**, which shows an antiferromagnetic behavior, the magnetism of the ferrous wheel **9** points to a ferromagnetic coupling (Figure 9). However, in neither case were we able to derive the coupling constants from these magnetic studies. Because these compounds are very air and moisture sensitive, paramagnetic impurities cannot be excluded. In order to shed light onto the somewhat complex magnetic properties of these wheel-shaped molecules, quantum chemical studies were performed.

Density functional theory (DFT) calculations on the hexanuclear complexes **8** and **9** were carried out in order to investigate the different types of spin–spin couplings, which are related to the energy differences between states of different spin. Since the splitting can be very sensitive to the amount of exact exchange admixture in the density functional,[33] both the pure BP86 and the hybrid B3LYP density functionals were employed for the [Fe_6] and [Mn_6] clusters.

For the description of the magnetic behavior, the interaction of the metal centers and, hence, their local spin configurations are of interest. Quantitative information on the spin distribution can be extracted from the local expressions for the expectation values of S_z and S^2. Note that $<S^2>$ is the square of the length of the total spin vector, whereas $<S_z>$ is the expectation value of the spin projected onto the z axis.

In order to devise the local spin operators, the total spin can be partitioned by using projection operators and assigned to atoms or groups of atoms. This may be accomplished by decomposition schemes according to Clark and Davidson[22] or according to Mayer.[23] In Mayer's approach, the local spin expectation values $<S_A{}^2>$ can be interpreted in terms of the local spin quantum number S_A as $S_A(S_A+1)$.[23b]

Because local S_{zA} expectation values do not depend on the decomposition scheme employed and, hence, yield the same results in Mayer's and in Clark and Davidson's analyses, we restrict ourselves to studying local $<S_{zA}>$ values. A derivation of the decomposition of S_z by using projection operators can be obtained as follows. The S_z operator is defined as the sum over one-electron operators s_z, see Equation (6).

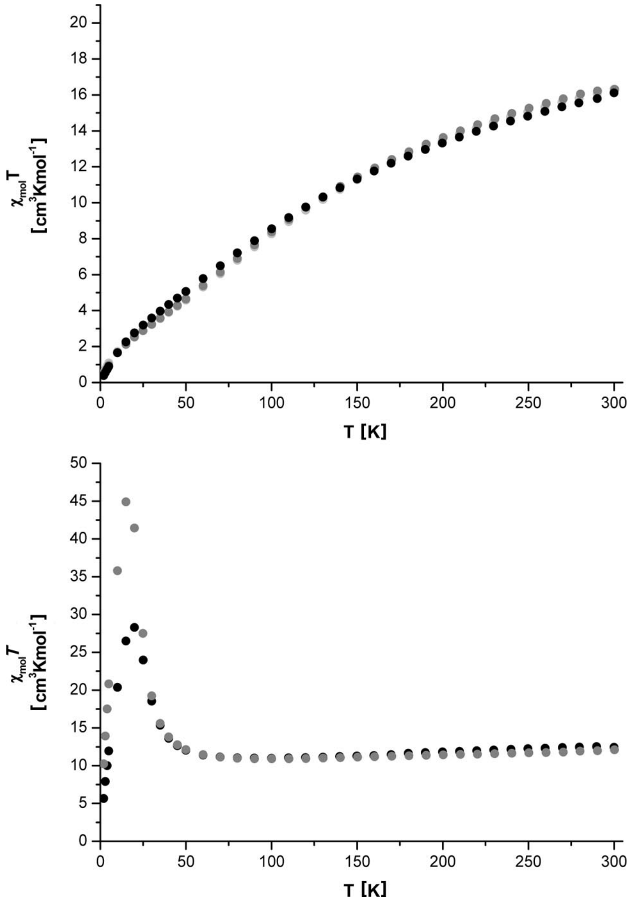

Figure 9. Temperature dependency of the susceptibility shown in a plot of $\chi_{mol}T$ vs. T for [Mn_6] (top) and of [Fe_6] (bottom) at applied fields of 1 kOe (grey, only for [Mn_6]), 2 kOe (light grey), and 5 kOe (black).

$$\hat{S}_z = \sum_i \hat{s}_z(i) \tag{6}$$

By introducing projection operators, p_A, defined by atom-centered basis functions, the cluster is divided into local basins A. They do not change any total expectation value because their sum equals the identity operator as shown in Equation (7).

$$\sum_A \hat{p}_A = \hat{1} \tag{7}$$

With the help of projection operators, S_z can be rewritten as the sum of local operators defined on basins A [Equation (8)].

$$\hat{S}_z = \sum_i \hat{s}_z(i) = \sum_{A,i} \hat{p}_A \hat{s}_z(i) = \sum_{A,i} \hat{s}_{zA}(i) = \sum_A \hat{S}_{zA} \tag{8}$$

The expectation value $<S_{zA}>$ can be calculated as the sum over one-electron integrals for the α- and β spin orbitals, denoted by $|i>$ and $|\text{-}i>$, respectively [Equation (9)], where the local $<S_{zA}>$ value is finally expressed in terms of the number of α-electrons $N^{\alpha}{}_{A}$ and β-electrons $N^{\beta}{}_{A}$ in basin A. The local spins are hence equal to half of the α spin electron excess on a given basin A.

$$\langle \hat{S}_{zA} \rangle = \sum_{i}^{N^{\alpha}} \langle i|\hat{p}_A(i)\hat{s}_z|i\rangle + \sum_{i}^{N^{\beta}} \langle \bar{\imath}|\hat{p}_A(i)\hat{s}_z|\bar{\imath}\rangle = \frac{1}{2}\left(N_A^{\alpha} - N_A^{\beta}\right) \tag{9}$$

The investigation of the local spin properties ensures that the converged orbitals describe the desired spin state. For our purpose, two spin states are of interest,[24,34] the high-spin state, describing ferromagnetic coupling of the metal centers, and the broken-symmetry state, which we refer to as the antiferromagnetically coupled state. In order to converge the determinant describing the desired local spin distribution, we employ our restrained optimization tool.[35] It constrains local spins to ideal S_z values, guides the optimization towards the region with the desired local properties, and subsequently relaxes the constraints so that a determinant corresponding to a true energy minimum is converged.

By considering the [Mn_6] cluster, both density functionals predict an antiferromagnetically coupled ($S = 0$) ground state for [Mn_6] with an energy difference to the ferromagnetically coupled ($S = 15$) state of –37.7 kJ mol^{-1} (BP86) (A) and –19.4 kJ mol^{-1} (B3LYP) (E) for single-point calculations on the X-ray crystal structure, which are from now on denoted as BP86//crystal and B3LYP//crystal (see Figure 10).

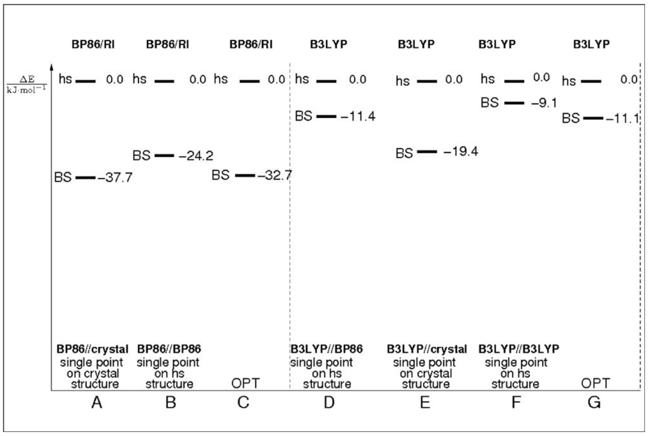

Figure 10. Relative energy splitting Δ*E* [kJ/mol] between the ferromagnetically coupled high-spin (hs) and the antiferromagnetically coupled broken-symmetry (BS) state of [Mn_6] (**8**) for the BP86 density functional (A–C) and the B3LYP density functional (D–G). In all calculations for [Mn_6], the antiferromagnetically coupled state is favored.

If both structures (the high-spin and broken-symmetry structures) are optimized with BP86, the relative stability of the antiferromagnetically coupled state decreases to –32.7 kJ mol^{-1} (C) for the BP86 density functional and to –11.1 kJ mol^{-1} (G) for the B3LYP functional. Furthermore, single-point calculations performed on the BP86-optimized high-spin state [denoted by (BP86//BP86) and (B3LYP//BP86)] also favor the broken-symmetry state by –24.2 kJ mol^{-1} (B) and by –11.4 kJ mol^{-1} (D), respectively. Even if a single-point calculation is performed on the B3LYP-optimized high-spin state, the antiferromagnetically coupled state is still more stable (F) by –9.1 kJ mol^{-1}.

From these calculations it can be seen that although both density functionals predict the same magnetic coupling, the energy splitting between the high-spin and the broken-symmetry state depends on the admixture of the exact Hartree–

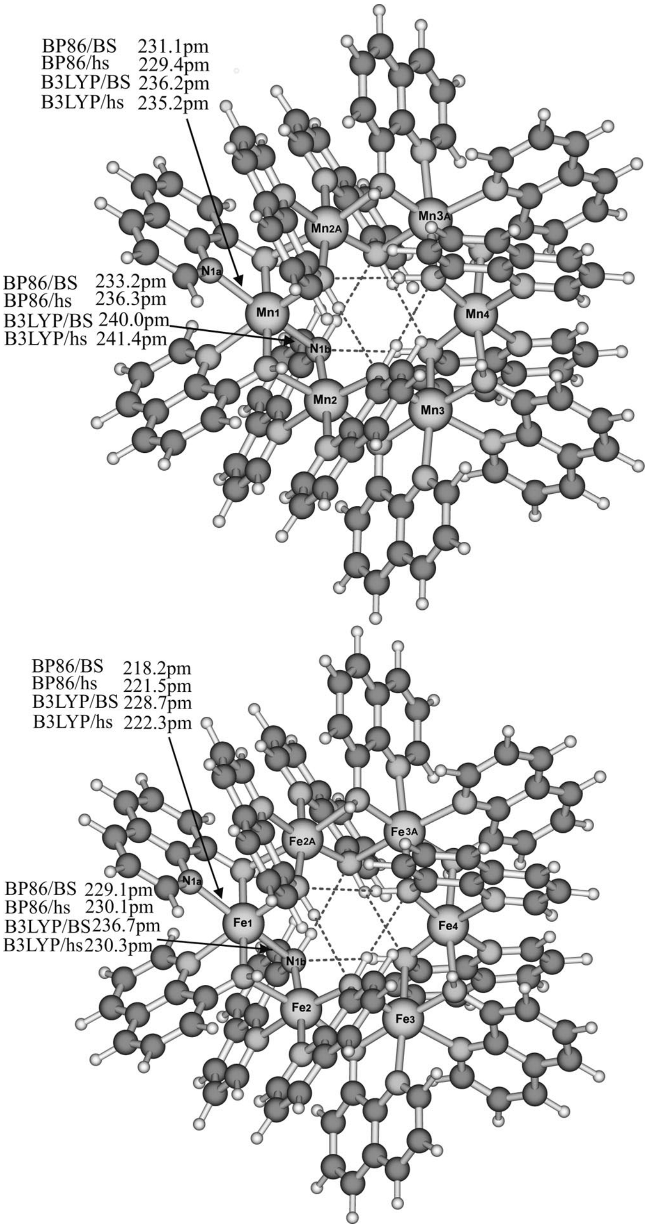

Figure 11. Optimized structures of [Mn_6] (**8**) and [Fe_6] (**9**). Selected bond lengths [pm] to bridging and non-bridging nitrogen atoms are given for the different optimized structure. BS denotes the antiferromagnetically coupled broken-symmetry state, whereas hs denotes the ferromagnetically coupled high-spin state. Note that the inner dotted lines are drawn to highlight the cage-like structure of the clusters.

Fock exchange energy in the density functional employed as one would have expected.[24,33]

All calculations are in agreement with experimental results, where an antiferromagnetic coupling is found. By considering the local spin properties, $S_{z\mathrm{Mn}}$ values between –2.35 and 2.36 a.u. are found for the manganese atoms in [$\mathrm{Mn_6}$], which are close to the ideal values of ±2.5 a.u. and correspond to local high-spin centers with 5 unpaired electrons. These values indicate that spin delocalization is small and that the correct high-spin and broken-symmetry Slater determinants have been converged.

The BP86-optimized most-stable [$\mathrm{Mn_6}$] broken-symmetry structure is presented in Figure 11, where selected bond lengths are presented for the various structure optimizations.

By considering all relevant bond lengths and angles, as displayed in Table 5, it can be seen that both the optimized high-spin and the broken-symmetry states are quite similar and are in agreement with the experimental X-ray crystal structure. The B3LYP-optimized structure has slightly larger bond lengths. The high-spin as well as the broken-symmetry state both contain local high-spin Mn centers. Hence, bond lengths in both the broken-symmetry and the high-spin structure are significantly larger than in the low-spin case. In the simple picture of ligand-field theory, this is due to the occupation of anti-bonding d orbitals.

The results for the [$\mathrm{Fe_6}$] complex are less unambiguous. Single-point calculations on the X-ray crystal structure (BP86//crystal) yield an energy gap of –24.1 kJ mol^{-1} (A) in favor of the antiferromagnetically coupled broken-symmetry state (S = 0) state when the BP86 density functional is used and an energy gap of –11.0 kJ mol^{-1} (D) for the B3LYP functional.

The BP86 structure optimization favors the ferromagnetically coupled state by –5.7 kJ mol^{-1} (C). For the single-point calculation on the BP86-optimized ferromagnetically coupled high-spin (S = 12) state, the relative stability of the ferromagnetically coupled state increases to –38.4 kJ mol^{-1} (B), denoted by BP86//BP86 in Figure 12, relative to the antiferromagnetically coupled broken-symmetry state. The B3LYP calculations, on the other hand, all predict the antiferromagnetically coupled (S = 0) spin state to be more stable. The structure optimization yields a broken-symmetry state that is –5.3 kJ mol^{-1}(F) more stable than the ferromagnetically coupled high-spin state, whereas the single-point calculation on the optimized high-spin state (B3LYP//B3LYP) (E) favors the antiferromagnetically coupled state by –3.2 kJ mol^{-1}. However, the energy splittings are quite small and may very well be the error of margin of DFT.

The BP86 density functional calculation fails, however, to reproduce the correct high-spin structure, and, instead, it turns out to be very much distorted relative to the X-ray crystal structure. This is illustrated when the relevant bond lengths and angles between the optimized ferromagnetically and antiferromagnetically coupled states are compared (see Table 6). Notable differences can be seen for the BP86 calculations. The wheel-like structure of the [$\mathrm{Fe_6}$] high-spin

Table 5. Selected bond lengths [pm] and bond angles [°] of the [$\mathrm{Mn_6}$] cluster (**8**) of the BP86-optimized antiferromagnetically coupled broken-symmetry (BS) state with $S = 0$ and ferromagnetically coupled high-spin (hs) state with $S = 15$; the experimental values determined by X-ray crystallography are included for comparison. Metal–ligand bonds to bridging nitrogen atoms are indicated by the index b, whereas bonds to non-bridging ligands are marked by the suffix a.

	BP86				B3LYP				Exp.
	BS	$<S_{z\mathrm{Mn}}>$	hs	$<S_{z\mathrm{Mn}}>$	hs	$<S_{z\mathrm{Mn}}>$	BS	$<S_{z\mathrm{Mn}}>$	
Mn1–N1a	231.1	2.23	229.4	2.28	235.2	2.35	236.2	2.34	227.3
Mn1–$\mathrm{N_{1b}}$	233.2		236.3		241.4		240.0		231.0
Mn2–N2a	232.9	–2.28	229.9	2.31	234.5	2.36	235.5	–2.35	228.8
Mn2–N2b	219.1		219.6		220.5		220.4		211.7
Mn3–N3a	230.8	2.23	229.1	2.27	234.9	2.35	235.5	2.34	228.3
Mn3–N3b	234.6		239.1		243.1		241.2		234.5
Mn4–N4a	232.3	–2.28	229.4	2.31	233.9	2.36	234.7	–2.35	227.4
Mn4–N4a′	232.1		229.4		233.9		234.6		227.4
Mn4–N3b′	239.2		245.8		247.8		246.1		245.0
Mn4–N4b	238.7		243.8		247.8		246.5		245.0
Mn3A–N3Aa	230.5	2.23	228.8	2.27	234.5	2.35	235.3	2.34	228.2
Mn3A–N3Ab	232.8		235.7		241.1		239.1		234.2
Mn2A–N2Aa	232.3	–2.28	229.4	2.31	234.3	2.36	235.3	–2.35	228.8
Mn2A–N2Ab	236.1		239.5		244.5		243.3		237.7
N1b–Mn1–N1b′	91.3		89.1		88.5		89.4		90.8
N1b–Mn2–N1b′	89.3		87.1		87.1		88.0		88.5
N2b–Mn2–N2b′	89.2		87.1		90.4		88.0		89.6
N2b–Mn3–N2b′	91.3		89.2		88.5		89.4		90.2
N3b–Mn3–N3b′	91.1		89.0		88.5		89.3		89.6
N3b–Mn4–N3b′	88.7		86.2		86.7		87.5		86.8
N4b–Mn4–N4b′	91.5		86.4		86.7		87.5		86.8
N4b–Mn3A–N4b′	91.3		89.2		88.4		89.3		89.6
N3Ab–Mn3A–N3Ab′	91.6		89.3		88.7		89.8		90.2
N3Ab–Mn2A–N3Ab′	89.4		87.2		87.3		88.2		89.6
N2Ab–Mn2A–N2Ab′	89.4		87.2		87.1		88.1		88.5
N2Ab–Mn1–N2Ab′	91.3		89.1		88.5		89.5		90.8

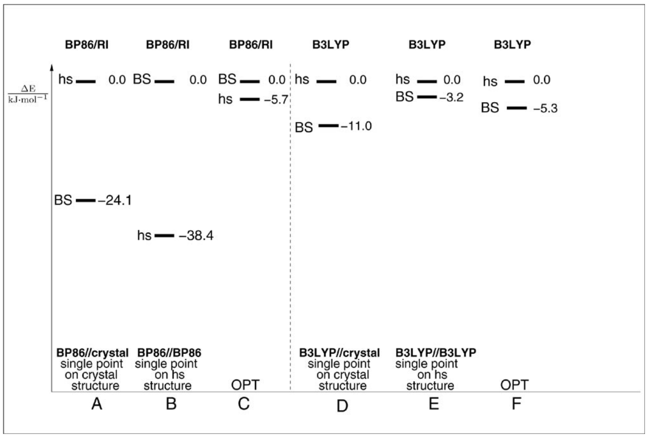

Figure 12. Relative energy differences for the [Fe$_6$] cluster (**9**) performed with the BP86 (A–C) and the B3LYP (C–F) density functionals. Single-point calculations on the X-ray crystal structure favor the antiferromagnetically coupled (S = 0) state [see (A) and (D)] for both density functionals. For single-point calculations on the optimized ferromagnetically coupled high-spin (S = 12) structure, BP86 favors a ferromagnetically coupled ground state (B), whereas for the B3LYP functional, an antiferromagnetically coupled state is slightly more stable for single-point calculations (E) and structure optimization (F).

state is less regular than that of the broken-symmetry state. Some Fe–N bond lengths of the high-spin structure, in particular Fe4–N4b, differ significantly from those of the broken-symmetry and the X-ray crystal structures. The B3LYP calculation solves this structural deficiency and yields a more regular high-spin structure with bond lengths and bond angles in good agreement with those of the experimental structure (see also Table 6). The structure of the [Fe$_6$] cluster as well as selected bond lengths for the BP86 and the B3LYP structure optimizations are displayed in Figure 11. However, given the limited accuracy of the standard density functional calculations, it cannot be determined which of the two states is the magnetic ground state. Also, the experimental measurements do not provide an unambiguous picture of the magnetic coupling.

For [Fe$_6$] local spin, values between –1.84 and 1.85 a.u. are found for the BP86 and B3LYP calculations that are close to the ideal value of ±2.0 a.u. (four unpaired electrons), which indicates that spin delocalization as well as spin pairing is small for both density functionals. This is in agreement with ligand field theory, where the tendency for spin pairing and the formation of low-spin complexes is less pronounced for 3d transition metals in a low oxidation state, such as Fe^{2+} in [Fe$_6$], because of a weak d orbital ligand field splitting.

Reaction Energies

Reaction energies for the structure-optimized clusters [Mn$_6$] and [Fe$_6$] can be calculated from the compounds shown in Equation (4) at 0 K without zero-point energy corrections. The metal complex MR$_2$ was chosen to be in the high-spin state with a spin state of S = 2.5 a.u. for MnR$_2$ and S = 2.0 a.u. for FeR$_2$. All reactions are found to be exothermic and reaction energies are of the same or-

Table 6. Selected bond lengths [pm] and bond angles [°] of [Fe$_6$] (**9**) for different spin states calculated for the BP86 and the B3LYP density functionals, as well as those for the experimental structure determined by X-ray crystallography. The broken-symmetry (BS) state with S = 0 describes antiferromagnetic coupling, whereas the high-spin (hs) state, where S = 12, describes ferromagnetic coupling.

	BP86				B3LYP				Exp.
	BS	S_{zFe}	hs	S_{zFe}	hs	S_{zFe}	BS	S_{zFe}	
Fe1–N1a	218.2	1.78	221.5	1.77	222.3	1.85	228.7	1.84	219.4
Fe1–N1b	229.1		230.1		230.3		236.7		228.3
Fe2–N2a	228.1	–1.76	227.3	1.81	223.9	1.85	232.3	–1.84	224.2
Fe2–N2b	212.1		212.8		212.4		214.4		211.9
Fe3–N3a	217.6	1.77	226.9	1.78	221.6	1.85	228.1		219.6
Fe3–N3b	230.8		219.6		234.3		237.5		231.1
Fe4–N4a	227.8	–1.75	232.5	1.79	223.5	1.85	231.7	1.84	224.0
Fe4–N4a′	228.0		218.7		223.8		231.6		224.0
Fe4–N3b′	235.0		214.9		239.4		238.8		239.5
Fe4–N4b	235.7		314.4		239.4		238.9		239.5
Fe3A–N3Aa	217.4	1.77	216.0	1.80	221.5	1.85	228.2	–1.84	219.7
Fe3A–N3Ab	227.5		235.0		229.8		235.4		229.8
Fe2A–N2Aa	228.2	–1.76	223.0	1.80	223.8	1.85	232.2	1.84	224.2
Fe2A–N2Ab	231.0		200.1		230.5		236.6		229.8
N1b–Fe1–N1b′	90.0		90.1		88.0		88.1		89.3
N1b–Fe2–N1b′	88.7		96.1		97.8		87.4		88.3
N2b–Fe2–N2b′	89.2		84.8		87.0		87.5		88.8
N2b–Fe3–N2b′	90.5		87.8		87.8		88.4		89.1
N3b–Fe3–N3b′	89.9		102.1		88.7		88.0		89.7
N3b–Fe4–N3b′	88.0		102.8		87.3		87.0		87.2
N4b–Fe4–N4b′	87.8		75.4		87.3		87.0		87.2
N4b–Fe3A–N4b′	89.7		92.0		88.8		88.0		89.7
N3Ab–Fe3A–N3Ab′	90.4		89.8		87.9		88.5		89.1
N3Ab–Fe2A–N3Ab′	89.1		82.4		87.1		87.6		88.8
N2Ab–Fe2A–N2Ab′	88.7		98.8		87.8		87.4		88.3
N2Ab–Fe1–N2Ab′	90.0		100.1		88.3		88.2		89.3

der of magnitude for [Mn_6] and [Fe_6] for both the BP86 and the B3LYP density functionals. For [Fe_6], a reaction energy of –1031.9 kJ mol^{-1} is found for the BP86-optimized broken-symmetry structure (BP86//BS), which corresponds to reaction energies of –172.0 kJ mol^{-1} per (BP86//BS) monomer. The B3LYP optimization of [Fe_6] yields a slightly higher reaction energy of –1128.2 kJ mol^{-1} for the formation of the high-spin structure (B3LYP//hs) and –1133.5 kJ mol^{-1} for the broken-symmetry structure (B3LYP//BS), which corresponds to –188.0 kJ mol^{-1} per (B3LYP//hs) monomer and –188.9 kJ mol^{-1} per (B3LYP//BS) monomer. For the BP86 structure optimization of [Mn_6], reaction energies of –1040.8 kJ mol^{-1} for the high-spin (BP86//hs) and –1073.5 kJ mol^{-1} for the broken-symmetry (BP86//BS) states are found, which correspond to –173.5 kJ mol^{-1} (BP86//hs) and –178.9 kJ mol^{-1} (BP86//BS) per monomer. The B3LYP structure optimizations yield reaction energies of –1224.0 kJ mol^{-1} (B3LYP//hs) and –1235.1 kJ mol^{-1} (B3LYP//BS), which give reaction energies of –204.0 kJ mol^{-1} (B3LYP//hs) and –205.9 kJ mol^{-1} (B3LYP//BS) per monomer.

Conclusions

The transamination reaction of M[N($SiMe_3$)$_2$]$_2$ with arylamines such as 8-aminoquinoline and 8-(trialkylsilylamino)quinoline yields the corresponding amidoquinolines with the metals manganese(II), iron(II), and cobalt(II). Trialkylsilyl-substituted amido groups avoid bridging positions between the two metal atoms because of a reduced basicity of the N-centered lone pair. These amido groups favor terminal positions, which allow a trigonal-planar geometry of the sp^2-hybridized amide function, stabilized by hyperconjugative backdonation of charge from the p_z(N) orbital to a σ*(Si–C) orbital of the trialkylsilyl group. This fact might be the reason that a 1:1 stoichiometry of M[N($SiMe_3$)$_2$]$_2$ (M = Mn, Fe, and Co) and 8-(trialkylsilylamino)quinoline also yields the 1:2 product, the bis[8-(trialkylsilylamido)quinoline]metal(II) complexes of these 3d transition metals, which leaves half of the amount of M[N($SiMe_3$)$_2$]$_2$ unreacted. However, the lack of trialkylsilyl groups at the 8-aminoquinoline group allows a stepwise transamination of M[N($SiMe_3$)$_2$]$_2$ (M = Mn, Fe, and Co). The amido function of the amidoquinoline ligand in bis[8-amidoquinoline metal(II) bis(trimethylsilyl)amide] occupies the bridging position between the metal atoms, which leads to coordination numbers of 4 for the metal and the amido N atoms. The transamination of (thf)Cr[N($SiMe_3$)$_2$]$_2$ with 8-aminoquinoline was not possible.

The molecular structures depend on the radius of the metal cations. A striking difference was found for the homoleptic bis(8-amidoquinoline)metal(II) complexes. The derivatives of zinc[4] are monomeric and show metal atoms in a distorted tetrahedral environment, the monomeric nickel derivative shows a square-planar arrangement of the Lewis bases as a result of strong ligand field stabilization. In contrast to these complexes with tetracoordinate metal atoms, the Mn and Fe complexes form hexamers with the metals in a distorted octahedral environment. These hexamers consist of metal-centered N_6 octahedrons, which are interconnected through common edges to form wheel-like molecular structures.

The reaction energies per monomer are between –172.0 and –188.9 kJ mol^{-1} for the formation of [Fe_6] and between –173.4 and –205.9 kJ mol^{-1} for [Mn_6]. The antiferromagnetic coupling of [Mn_6] predicted by DFT calculations confirm the experimental data. The situation is less clear in the case of [Fe_6] because of the very close-lying ferromagnetically and antiferromagnetically coupled states.

Experimental Section

All manipulations were performed in an argon atmosphere. Solvents were dried and distilled according to common procedures. The IR spectra were recorded as Nujol solutions between KBr windows. Starting materials (thf)$_2$Cr[N($SiMe_3$)$_2$]$_2$, M[N($SiMe_3$)$_2$]$_2$ (M = Mn, Fe, Co), 8-(triisopropylsilyl)quinoline, and 8-(*tert*-butyldimethylsilyl)quinoline were prepared according to literature procedures. For the interpretation of the mass spectra, the abbreviation "ach" stands for the aminoquinolyl fragment $C_9N_2H_7$.

Synthesis of Bis[8-(*tert*-butyldimethylsilylamido)quinoline]chromium(II) (1): A solution of (thf)$_2$Cr[N($SiMe_3$)$_2$]$_2$ (0.86 g, 1.70 mmol) in ethyl ether (15 mL) was layered with a solution of *N*-*tert*-butyldimethylsilyl-8-aminoquinoline (0.86 g, 3.33 mmol) in ether (15 mL). At the boundary layer, the color changed immediately to brown–violet. Diffusion within this unstirred reaction mixture led to the precipitation of black needleshaped crystals of **1**. The crystals were collected, washed with diethyl ether, and dried in vacuo. Yield: 0.67 g (1.2 mmol, 71%). M.p. 296 °C. IR (Nujol): ṽ = 1557 (m), 1494 (s), 1421 (m), 1360 (m), 1311 (vs), 1278 (m), 1257 (m), 1247 (m), 1220 (m), 1113 (s), 1075 (w), 1041 (w), 1004 (w), 932 (m), 856 (m), 828 (br. s), 804 (m), 789 (s), 742 (m), 666 (m), 647 (w), 632 (w), 572 (w), 532 (m), 523 (m), 457 (w) cm^{-1}. MS (DEI): *m*/*z* (%) = 567 (2) [M$^+$], 551 (2) [M – Me]$^+$, 509 (2) [M – *t*Bu]$^+$, 258 (75) [achSiMe$_2$*t*Bu]$^+$, 200 (75) [achSiMe$_2$ – H]$^+$, 171 (100) [achSi]$^+$. Magnetism: μ_{eff} = 4.5 μ_B at 18.0 °C. $C_{30}H_{42}CrN_4Si_2$ (566.85): calcd. C 63.57, H 7.47, N 9.88; found C 62.70, H 7.56, N 9.72.

Synthesis of Bis[8-(*tert*-butyldimethylsilylamido)quinoline]manganese(II) (2a): A solution of Mn[N($SiMe_3$)$_2$]$_2$ (0.26 g, 0.69 mmol) in ethyl ether (15 mL) was cooled to –20 °C. *N*-*tert*-butyldimethylsilyl-8-aminoquinoline (0.36 g, 1.39 mmol) was then added to the stirred solution. After a few minutes, the reaction mixture turned dark brown. At –18 °C, 0.21 g of yellow cuboids of **2a** precipitated (0.37 mmol, 54%). M.p. 210 °C. IR (Nujol): ṽ = 1568 (m), 1507 (m), 1496 (m), 1418 (w), 1361 (m), 1315 (s), 1280 (m), 1254 (m), 1230 (w), 1112 (s), 1096 (w), 1042 (w), 1006 (w), 934 (m), 914 (w), 835 (vs), 819 (m), 787 (s), 741 (m), 664 (m), 647 (w), 572 (w), 523 (w) cm^{-1}. MS (DEI): *m*/*z* (%) = 569 (29) [M$^+$], 554 (6) [M – Me]$^+$, 512 (76) [M – *t*Bu]$^+$ 258 (27) [achSiMe$_2$*t*Bu]$^+$, 200 (100) [achSiMe$_2$ – H]$^+$, 171 (22) [achSi]$^+$. Magnetism: μ_{eff} = 5.6 μ_B at 26.9 °C. $C_{30}H_{42}MnN_4Si_2$ (569.79): calcd. C 63.24, H 7.43, N 9.83; found C 61.36, H 7.18, N 9.70.

Synthesis of Bis[8-(triisopropylsilylamido)quinoline]manganese(II) (2b): *N*-triisopropylsilyl-8-aminoquinoline (0.49 g, 1.62 mmol) was added dropwise to a stirred solution of Mn[N($SiMe_3$)$_2$]$_2$ (0.30 g, 0.81 mmol) in thf (8 mL) at –20 °C. Within a few days, 0.14 g of orange–yellow crystals of **2b** (0.22 mmol, 27%) precipitated from this oily solution. M.p. 137 °C. IR (Nujol): ṽ = 1613 (w), 1573 (m), 1508 (s), 1416 (m), 1324 (s), 1231 (w), 1096 (m), 1015 (w), 912 (m), 882 (m), 819 (m), 807 (m), 789 (s), 741 (m), 727 (m), 675 (m), 571 (w), 502 (w) cm^{-1}. MS (DEI): *m*/*z* (%) = 653 (2) $[M^+]$, 610 (5) [M – *i*Prop]$^+$, 301 (47) [ach*i*Prop$_3$]$^+$, 255 (34) [ach*i*Prop$_2$ – H]$^+$, 172 (32) [achSiH]$^+$, 43 (100) [*i*Prop]$^+$. Magnetism: μ_{eff} = 5.65 μ_B at 27.0 °C. $C_{36}H_{54}MnN_4Si_2$ (653.95): calcd. C 66.32, H 8.35, N 8.29; found C 65.70, H 8.59, N 8.43.

Synthesis of Bis[8-(*tert*-butyldimethylsilylamido)quinoline]iron(II) (3a): Method A: A solution of $[Fe\{N(SiMe_3)_2\}_2]_2$ (0.31 g, 0.41 mmol) in ethyl ether (5 mL) was cooled to –78 °C. A solution of *N*-*tert*-butyldimethylsilyl-8-aminoquinoline (0.42 g, 1.64 mmol) in ethyl ether (5 mL) was then added slowly. After complete addition, the reaction mixture was warmed to room temperature. Thereafter, 0.35 g of red needles of **3a** (0.62 mmol, 76%) precipitated, which were isolated and dried in vacuo. Method B: A solution of $[Fe\{N(SiMe_3)_2\}_2]_2$ (0.41 g, 0.60 mmol) in ether (5 mL) was layered with a solution of *N*-*tert*-butyldimethylsilyl-8-aminoquinoline (0.57 g, 2.20 mmol) in ether (8 mL). Diffusion led to formation of red needleshaped crystals, which were collected, washed with diethyl ether and dried in vacuo. Yield: 0.51 g (0.9 mmol, 81%). M.p. 239 °C. IR (Nujol): ṽ = 1568 (m), 1494 (m), 1314 (s), 1278 (m), 1248 (m), 1112 (s), 1074 (w), 1040 (w), 1006 (w), 935 (m), 835 (br. m), 818 (m), 804 (w), 788 (s), 742 (m), 666 (m), 646 (w), 634 (w), 572 (w), 532 (w) cm^{-1}. MS (DEI): *m*/*z* (%) = 570 (5) $[M^+]$, 555 (2) [M – Me]$^+$, 513 (7) [M – *t*Bu]$^+$ 258 (19) [achSiMe$_2$*t*Bu]$^+$, 201 (100) [achSiMe$_2$]$^+$, 171 (31) [achSi]$^+$. Magnetism: μ_{eff} = 4.75 μ_B at 21.0 °C. $C_{30}H_{42}FeN_4Si_2$ (570.70): calcd. C 63.14, H 7.42, N 9.82; found C 63.88, H 7.18, N 9.55.

Synthesis of Bis[8-(triisopropylsilylamido)quinoline]iron(II) (3b): A solution of *N*-triisopropylsilyl-8-aminoquinoline (0.59 g, 1.96 mmol) in ethyl ether (10 mL) was added dropwise to a solution of $[Fe\{N(SiMe_3)_2\}_2]_2$ (0.36 g, 0.49 mmol) in Et_2O (10 mL) that was cooled to –78 °C. After complete addition, the reaction mixture was warmed to room temperature and stirred for an additional 17 h. The volume of the solution was then reduced to half of the original volume. The small red crystals of **1b** (0.27 g, 0.42 mmol, 43%) that precipitated were isolated and dried in vacuo. M.p. 132 °C. IR (Nujol): ṽ = 1563 (m), 1508 (w), 1495 (m), 1311 (s), 1274 (m), 1222 (w), 1111 (m), 1074 (w), 1041 (w), 1012 (w), 927 (m), 881 (m), 818 (s), 789 (m), 755 (m), 741 (m), 670 (br. w), 647 (w), 588 (w), 559 (w), 531 (w), 500 (w) cm^{-1}. MS (DEI): *m*/*z* (%) = 654 (2) $[M^+]$, 611 (2) [M – *i*Pr]$^+$, 300 (28) [ach*i*Pr$_3$]$^+$, 257 (100) [ach*i*Prop$_2$]$^+$, 171 (74) [achSi]$^+$. $C_{36}H_{54}FeN_4Si_2$ (652.96): calcd. C 66.22, H 8.34, N 8.27; found C 65.99, H 8.38, N 8.23.

Synthesis of Bis[8-(*tert*-butyldimethylsilylamido)quinoline]cobalt(II) (4a): A solution of $[Co\{N(SiMe_3)_2\}_2]_2$ (0.62 g, 0.82 mmol) in toluene (4 mL) was cooled to –78 °C. A solution of *N*-*tert*-butyldimethylsilyl-8-aminoquinoline (0.73 g, 2.82 mmol) in toluene (4 mL) was then added dropwise. After complete addition, the reaction mixture was warmed to room temperature and stirred for an additional hour. All volatile materials were then removed in vacuo. The brown–orange residue was shaken with hexane. The insoluble product was isolated by filtration. Yield: 0.61 g (1.07 mmol, 76%). M.p. 186 °C. IR (Nujol): ṽ = 1562 (m), 1494 (m), 1456 (vs), 1316 (s), 1280 (m), 1248 (m), 1114 (s), 1041 (w), 1006 (w), 938 (m), 833 (br. m), 818 (m), 786 (s), 742 (m), 666 (w), 646 (w), 572 (w), 532 (w), 455 (w) cm^{-1}. MS (DEI): *m*/*z* (%) = 574 (18) $[M^+]$, 559 (2) [M – Me]$^+$, 518 (27) [M – *t*Bu]$^+$, 258 (100) [achSiMe$_2$*t*Bu]$^+$, 201 (92) [achSiMe$_2$]$^+$, 171 (100) [achSi]$^+$. Magnetism: μ_{eff} = 4.26 μ_B at 22 °C. $C_{30}H_{42}CoN_4Si_2$ (573.79): calcd. C 65.92, H 8.30, N 8.24; found C 65.40, H 6.95, N 8.45.

Synthesis of Bis[8-(triisopropylsilylamido)quinoline]cobalt(II) (4b): At –78 °C, a solution of *N*-triisopropylsilyl-8-aminoquinoline (0.71 g, 2.40 mmol) in Et_2O (8 mL) was added dropwise to a solution of $[Co\{N(SiMe_3)_2\}_2]_2$ (0.46 g, 0.60 mmol) in ethyl ether (10 mL). After complete addition, the brown–orange mixture was stirred at room temperature for 3 h. During the reduction of the volume of the solution, a brown microcrystalline powder precipitated. The solution was filtered and from the filtrate another crop of brown crystals formed. Yield: 0.35 g (0.54 mmol, 45%). M.p. 233 °C. IR (Nujol): ṽ = 1566 (m), 1495 (m), 1363 (m), 1312 (vs), 1275 (m), 1222 (w), 1112 (s), 1075 (w), 1011 (w), 931 (m), 880 (w), 855 (w), 825 (m), 815 (m), 785 (m), 755 (m), 737 (m), 675 (w), 649 (w), 629 (w), 553 (w), 528 (w), 492 (w) cm^{-1}. MS (DEI): *m*/*z* (%) = 657 (11) $[M^+]$, 614 (32) [M – *i*Pr]$^+$, 571 (4) [M – 2*i*Pr]$^+$, 357 (12) [M – ach*i*Pr$_3$]$^+$, 300 (14) [ach*i*Pr$_3$]$^+$, 257 (91) [ach*i*Pr$_2$]$^+$, 171 (100) [achSi]$^+$. $C_{36}H_{54}CoN_4Si_2$ (655.95): calcd. C 62.80, H 7.38, N 9.76; found C 60.97, H 7.23, N 9.68.

Synthesis of Bis[8-amidoquinoline manganese(II)bis(trimethylsilyl)amide] (5): Manganese bis[bis(trimethylsilyl)amide] (0.46 g, 1.22 mmol) was dissolved in ethyl ether (20 mL) and cooled to –20 °C. Solid 8-aminoquinoline (0.18 g, 1.23 mmol) was added. After 5 min, all solids were removed, and the mother liquor stored at –18 °C. Within 24 h, 0.20 g of orange–yellow crystals of **5** (0.28 mmol, 45%) precipitated. This compound decomposed slowly at room temperature. IR: ṽ = 3380 (vw), 3317 (vw), 3277 (vw), 1594 (m), 1565 (m), 1502 (s), 1330 (m), 1268 (w), 1249 (m), 1178 (w), 1096 (m), 1064 (w), 1034 (w), 997 (m), 931 (m), 874 (w), 818 (m), 785 (m), 749 (m), 681 (w), 611 (w), 503 (w) cm^{-1}. Magnetism: μ_{eff} = 6.0 μ_B at 26.9 °C.

Synthesis of Bis[8-amidoquinoline iron(II)bis(trimethylsilyl)amide] (6): A solution of $[Fe\{N(SiMe_3)_2\}_2]_2$ (0.49 g, 0.66 mmol) in ethyl ether (10 mL) was cooled to –78 °C and layered by a solution of 8-aminoquinoline (0.19 g, 1.33 mmol) in Et_2O (10 mL). The Schlenk flask containing the two layers of the ether solutions was kept at –20 °C. Within 1 d, diffusion led to formation of 0.12 g of red needles of **6** (0.17 mmol, 25%) at the phase boundary. Decomposition above 50 °C. IR (Nujol): ṽ = 3366 (w), 3300 (w), 3250 (w), 1594 (w), 1567 (m), 1502 (vs), 1427 (m), 1343 (m), 1328 (m), 1248 (br. m), 1178 (w), 1103 (m), 1062 (w), 1034 (w), 980 (m), 931 (w), 872 (w), 818 (m), 804 (m), 785 (s), 680 (br. m), 643 (m), 520 (w) cm^{-1}. MS (DEI): *m*/*z* (%) = 146 (96) [HN(SiMe3)2 – Me]$^+$, 117 (88) [ach – C_2H_2]$^+$. Magnetism: μ_{eff} = 5.3 μ_B at 26.9 °C. $C_{30}H_{50}Fe_2N_6Si_4$ (718.79): calcd. C 50.13, H 7.01, N 11.69; found C 51.50, H 6.26, N 12.34.

Synthesis of Bis[8-amidoquinoline cobalt(II)bis(trimethylsilyl)amide] (7): A solution of $[Co\{N(SiMe_3)_2\}_2]_2$ (0.59 g, 0.78 mmol) in ethyl ether was cooled to –30 °C. A solution of 8-aminoquinoline (0.23 g, 1.60 mmol) was then added dropwise. Within one week, 0.35 g of brown crystals of **5** (0.48 mmol, 62%) formed in this cooled solution. Decomposition above 50 °C. IR (Nujol): ṽ = 3364 (w), 1592 (m), 1564 (s), 1502 (s), 1344 (m), 1305 (w), 1256 (w), 1102 (m), 815 (m), 803 (m), 781 (m), 731 (m), 645 (w), 540 (w), 518 (w) cm^{-1}. Magnetism: μ_{eff} = 4.3 μ_B at 26.9 °C. $C_{30}H_{50}Co_2N_6Si_4$ (724.97): calcd. C 49.70, H 6.95, N 11.59; found C 49.85, H 6.79, N 11.02.

Synthesis of Hexakis[bis(8-amidoquinoline)manganese(II)] (8): A solution of 8-aminoquinoline (0.32 g, 2.25 mmol) in Et_2O (10 mL) was added dropwise to a solution of $Mn[N(SiMe_3)_2]_2$ (0.40 g, 1.07 mmol) in Et_2O (10 mL) at –20 °C. Storage of this mixture at –18 °C led to the formation of dark brown crystals of **4** (0.29 g, 0.14 mmol, 79%). Mp. 251 °C. IR: ṽ = 3297 (m), 3283 (m), 3042 (m), 1596 (w), 1560 (s), 1502 (s), 1424 (m), 1362 (vs), 1333 (vs), 1275 (m), 1262 (m), 1216 (w), 1164 (w), 1099 (s), 1061 (w), 1037 (w), 868 (w), 817 (m), 804 (m), 789 (s), 754 (br. s), 717 (m), 700 (m), 653 (m), 592 (w), 552 (w), 487 (m) cm^{-1}. Magnetism: μ_{eff} = 11.4 μ_B at 26.9 °C. $C_{108}H_{84}Mn_6N_{24}$ (2047.65): calcd. C 63.35, H 4.13, N 16.42; found C 63.18, H 4.12, N 16.37.

Synthesis of Hexakis[bis(8-amidoquinoline)iron(II)] (9): A solution of $[Fe\{N(SiMe_3)_2\}_2]_2$ (0.40 g, 0.53 mmol) in ethyl ether (8 mL) was cooled to –78 °C. Very slowly, a solution of 8-aminoquinoline (0.3 g, 2.1 mmol) in ethyl ether (10 mL) was then added. This reaction mixture was stirred at –40 °C and then stored at –20 °C. Long black needles were obtained within a few days. Yield: 0.22 g (0.12 mmol, 60 %). M.p. 168 °C. IR (Nujol): $\tilde{\nu}$ = 3472 (w), 3371 (w), 3323 (w), 3284 (m), 1595 (m), 1564 (s), 1501 (s), 1424 (m), 1331 (s), 1276 (m), 1212 (w), 1099 (m), 1063 (w), 1033 (w), 854 (w), 817 (m), 802 (m), 786 (s), 748 (br. m), 683 (w), 650 (w), 587 (w), 495 (m) cm^{-1}. MS (DEI): *m/z* (%) = 144 (100) $[ach]^+$, 117 (74) $[ach - C_2H_3]^+$. Magnetism: μ_{eff} = 9.8 μ_B at 26.9 °C, μ_{eff} = 18.9 μ_B at –258.2 °C. $C_{108}H_{84}Fe_6N_{24}$ (2053.05): calcd. C 63.18, H 4.12, N 16.37; found C 61.78, H 4.04, N 15.99.

Synthesis of Bis(8-amidoquinoline)cobalt(II) (10): 8-Aminoquinoline (0.33 g, 2.27 mmol) was dissolved in ethyl ether (5 mL) and added to a solution of $[Co\{N(SiMe_3)_2\}_2]_2$ (0.43 g, 0.57 mmol) in ethyl ether (10 mL) at –78 °C. After complete addition, the solution was warmed to –20 °C and stored at this temperature. After 2 d, 0.30 g of a brownish black microcrystalline powder of **9** (0.85 mmol, 75 %) was collected and dried under vacuum. M.p. 275 °C (dec.). IR (Nujol): $\tilde{\nu}$ = 3364 (m), 1586 (m), 1599 (s), 1502 (vs), 1431 (m), 1343 (s), 1286 (w), 1223 (w), 1170 (w), 1111 (m), 1036 (w), 916 (w), 815 (m), 805 (m), 780 (m), 753 (m), 670 (m), 645 (m), 606 (w), 592 (m), 540 (m) cm^{-1}. MS (DEI): *m/z* (%) = 345 (85) $[M]^+$, 202(15) $[M - ach]^+$, 144 (100) $[ach]^+$, 117 (100) $[ach - C_2H_3]^+$. Magnetism: μ_{eff} = 2.3 μ_B at 26.9 °C. $C_{18}H_{14}CoN_4$ (345.26): calcd. C 62.60, H 4.07, N 16.23; found C 60.79, H 4.38, N 15.50.

Computational Methodology: All-electron DFT structure optimizations and local spin analyses were carried out with our local version of the TURBOMOLE 5.1 program package.[36] The BP86[37] and the B3LYP[38] density functionals were employed, in combination with Ahlrichs' triple-zeta basis set featuring one polarization function (TZVP) for the metal atoms and the split-valence basis set with one polarization function on each non-hydrogen atom [SV(P)], for the remaining atoms.[39] In order to investigate the local spin properties of the converged Kohn–Sham determinants, partial spins $<S_{zA}>$ were calculated by using a modified Löwdin partitioning scheme.[22,23]

X-ray Crystal Structure Determinations: The intensity data for the compounds were collected on a Nonius KappaCCD diffractometer by using graphite-monochromated Mo-K_α radiation. Data were corrected for Lorentz polarization effects and for absorption effects.[40–42] The crystal structures were solved by direct methods (SHELXS[43]) and refined by full-matrix least-squares techniques against F_o^2 (SHELXL-97[44]). Crystal data and refinement details for the X-ray structure determinations are listed in Tables 7 and 8. For compound **2a** and for all amine groups, the hydrogen atoms at N2 were located by difference Fourier synthesis and refined isotropically. The other hydrogen atoms were included at calculated positions with fixed thermal parameters. All non-disordered, non-hydrogen atoms were refined anisotropically.[44] XP (SIEMENS Analytical X-ray Instruments, Inc.) was used for structure representations. CCDC-680529 (**1**), -680530 (**2a**), -680531 (**2b**), -680532 (**3a**), -680533 (**3b**), -680534 (**4b**), -672193 (**5**), -672194 (**6**), -672195 (**7**), -672196 (**8**), and -672197 (**9**) contain the supplementary crystallographic data for this paper. These data can be obtained free of charge from The Cambridge Crystallographic Data Centre via www.ccdc.cam.ac.uk/data_request/cif.

Table 7. Crystal data and refinement details for the X-ray structure determinations for **1**–**4**.

	1	**2a**	**2b**	**3a**	**3b**	**4b**
Formula	$C_{30}H_{42}CrN_4Si_2$	$C_{30}H_{42}MnN_4Si_2$	$C_{36}H_{54}MnN_4Si_2$	$C_{30}H_{42}FeN_4Si_2$	$C_{36}H_{54}FeN_4Si_2$	$C_{36}H_{54}CoN_4Si_2$
F_w [$g mol^{-1}$]	566.86	569.80	653.95	570.71	654.86	657.94
T [°C]	–90(2)	–90(2)	–90(2)	–90(2)	–90(2)	–90(2)
Crystal system	monoclinic	monoclinic	triclinic	monoclinic	triclinic	monoclinic
Space group	*C*2/*c*	*C*2/*c*	$P\bar{1}$	*C*2/*c*	$P\bar{1}$	P2/n
a [Å]	19.4479(9)	19.2086(8)	12.4264(4)	19.0702(12)	12.3592(6)	20.9401(8)
b [Å]	7.7577(6)	8.1705(2)	17.8362(8)	8.1495(5)	17.7611(4)	8.8973(2)
c [Å]	20.6124(9)	20.0331(8)	18.3219(9)	20.1018(10)	18.3606(7)	21.3944(9)
α [°]	90.00	90.00	69.416(2)	90.00	69.129(2)	90.00
β [°]	104.565(4)	103.249(2)	71.012(2)	103.802(3)	71.648(2)	117.117(1)
γ [°]	90.00	90.00	85.492(3)	90.00	85.516(2)	90.00
V [$Å^3$]	3009.9(3)	3060.39(19)	3591.8(3)	3033.9(3)	3571.8(2)	3547.8(2)
Z	4	4	4	4	4	4
ρ [$g cm^{-3}$]	1.251	1.237	1.209	1.249	1.218	1.232
μ [cm^{-1}]	4.85	5.35	4.64	6.01	5.19	5.81
Measured data	9274	10495	24118	9942	23855	23357
Data with $I > 2\sigma(I)$	2275	2818	9155	2503	9757	5583
Unique data/R_{int}	3434/0.0678	3501/0.0443	15890/0.0586	3463/0.0758	15873/0.0455	8112/0.0569
wR_2 (all data, on F^2)[a]	0.1459	0.0947	0.1479	0.1237	0.1266	0.1076
R_1 [$I > 2\sigma(I)$][a]	0.0540	0.0376	0.0627	0.0468	0.0563	0.0436
s[b]	0.994	1.005	1.020	1.030	1.004	1.019
Residual density [$e Å^{-3}$]	1.217/–0.471	0.409/–0.235	0.399/–0.462	0.314/–0.507	0.360/–0.339	0.316/–0.377
Absorption method	multiscan	multiscan	multiscan	multiscan	multiscan	multiscan
Absorption corr. $T_{min/max}$	0.9179/0.9556	0.8983/0.9522	0.9153/0.9700	0.8600/0.9570	0.9104/0.9388	0.9073/0.9377

[a] Definition of the R indices: $R_1 = (\Sigma||F_o| - |F_c||)/\Sigma|F_o|$, $wR_2 = \{\Sigma[w(F_o^2 - F_c^2)^2]/\Sigma[w(F_o^2)^2]\}^{1/2}$ with $w^{-1} = \sigma^2(F_o^2) + (aP)^2$. [b] $s = \{\Sigma[w(F_o^2 - F_c^2)^2]/(N_o - N_p)\}^{1/2}$.

Table 8. Crystal data and refinement details for the X-ray structure determinations for **5**–**9**.

	5	**6**	**7**	**8**	**9**
Formula	$C_{30}H_{50}Mn_2N_6Si_4$	$C_{30}H_{50}Fe_2N_6Si_4$	$C_{30}H_{50}Co_2N_6Si_4$	$C_{108}H_{84}Mn_6N_{24}\cdot 5C_4H_{10}O$	$C_{108}H_{84}Fe_6N_{24}\cdot 5C_4H_{10}O$
F_w [g mol^{-1}	717.00	718.82	724.98	2418.23	2423.69
T [°C]	–90(2)	–90(2)	–90(2)	–90(2)	–90(2)
Crystal system	triclinic	triclinic	triclinic	monoclinic	monoclinic
Space group	$P\bar{1}$	$P\bar{1}$	$P\bar{1}$	$C2/c$	$C2/c$
a [Å]	8.7332(8)	8.7609(4)	8.7739(11)	14.1733(16)	14.2276(3)
b [Å]	9.5691(7)	9.6500(5)	9.6400(8)	29.892(3)	29.8008(6)
c [Å]	11.9411(8)	11.7060(5)	11.6137(14)	28.076(3)	27.8578(4)
α [°]	74.597(4)	74.826(3)	74.814(7)	90.00	90.00
β [°]	85.493(4)	85.188(3)	84.873(5)	100.027(7)	100.041(1)
γ [°]	72.647(4)	72.732(2)	72.893(7)	90.00	90.00
V [Å^3]	918.27(12)	912.08(7)	905.97(17)	11713(2)	11630.6(4)
Z	1	1	1	4	4
ρ [g cm^{-3}]	1.297	1.309	1.329	1.371	1.384
μ [cm^{-1}]	8.47	9.55	10.77	6.94	7.95
Measured data	6191	6260	6078	30975	37409
Data with $I > 2\sigma(I)$	2891	3312	2823	4674	8045
Unique data/R_{int}	4073/0.0352	4054/0.0240	4048/0.0582	13277/0.1954	13275/0.0720
wR_2 (all data, on F^2)$^{a)}$	0.1015	0.0906	0.1453	0.2673	0.1422
R_1 [$I > 2\sigma(I)$][a]	0.0453	0.0348	0.0560	0.1082	0.0554
s[b]	1.027	1.033	1.000	1.019	0.988
Residual density [e Å^{-3}]	0.326/–0.349	0.384/–0.449	0.540/–0.658	0.742/–0.457	1.103/–0.511
Absorption method	multiscan	multiscan	multiscan	multiscan	multiscan
Absorption corr. $T_{min/max}$	0.8712/0.8952	0.8258/0.866	0.7236/0.9587	0.8405/0.8838	0.8405/0.8838

[a] Definition of the R indices: $R_1 = (\Sigma||F_o| - |F_c||)/\Sigma|F_o|$, $wR_2 = \{\Sigma[w(F_o^2 - F_c^2)^2]/\Sigma[w(F_o^2)^2]\}^{1/2}$ with $w^{-1} = \sigma^2(F_o^2) + (aP)^2$. [b] $s = \{\Sigma[w(F_o^2 - F_c^2)^2]/(N_o - N_p)\}^{1/2}$.

Acknowledgments

This work was supported in the collaborative research initiative of the DFG (SFB 436) as well as by project WE 1561/9-1, and we are grateful to the Deutsche Forschungsgemeinschaft (DFG, Bonn-Bad Godesberg, Germany) for generous funding. We also acknowledge the support by the Fonds der Chemischen Industrie (Frankfurt/Main, Germany) and by the Swiss Science Foundation SNF (project no. 200021-113479/1) as well as by the ETH Zurich through TH grant 0-20436-07. A. M. thanks the Carl-Zeiss-Stiftung (Germany) for a generous Ph. D. grant. In addition we thank the Prof. W. Plass and Mrs. C. Felbel for performing the magnetic measurements.

---

[1] C. Koch, A. Malassa, C. Agthe, H. Görls, R. Biedermann, H. Krautscheid, M. Westerhausen, *Z. Anorg. Allg. Chem.* **2007**, *633*, 375–382.

[2] L. M. Englehardt, P. C. Junk, W. C. Patalinghug, R. E. Sue, C. L. Raston, B. W. Skelton, A. H. White, *J. Chem. Soc., Chem. Commun.* **1991**, 930–932.

[3] a) H. K. Lee, Y. Peng, S. C. F. Kui, Z.-Y. Zhang, Z.-Y. Zhou, T. C. W. Mak, *Eur. J. Inorg. Chem.* **2000**, 2159–2162; b) A. Malassa, B. Jäger, H. Görls, M. Westerhausen, *Acta Crystallogr., Sect. E* **2010**, *66*, m6.

[4] A. Malassa, C. Koch, B. Stein-Schaller, H. Görls, M. Friedrich, M. Westerhausen, *Inorg. Chim. Acta* **2008**, *361*, 1405–1414.

[5] a) C. Engelter, G. E. Jackson, C. L. Knight, D. A. Thornton, *J. Coord. Chem.* **1989**, *20*, 297–306; b) J. C. Fanning, L. T. Taylor, *J. Inorg. Nucl. Chem.* **1965**, *27*, 2217–2223; c) R. Nast, H. Bier, J. Gremm, *Z. Anorg. Allg. Chem.* **1961**, *309*, 289–296.

[6] D. C. Bradley, M. H. Chisholm, *Acc. Chem. Res.* **1976**, *9*, 273–280.

[7] G. Mezei, C. M. Zaleski, V. L. Pecoraro, *Chem. Rev.* **2007**, *107*, 4933–5003.

[8] Only a selection is given: a) A. M. Ako, H. Maid, S. Sperner, S. H. H. Zaidi, R. W. Saalfrank, M. S. Alam, P. Müller, F. W. Heinemann, *Supramol. Chem.* **2005**, *17*, 315–321. R; b) W. Saalfrank, C. Deutscher, S. Sperner, T. Nakajima, A. M. Ako, E. Uller, F. Hampel, F. W. Heinemann, *Inorg. Chem.* **2004**, *43*, 4372–4382; c) C. Canada-Vilalta, M. Pink, G. Christou, *Chem. Commun.* **2003**, 1240–1241; d) L. F. Jones, A. Batsanov, E. K. Brechin, D. Collison, M. Helliwell, T. Mallah, E. J. L. McInnes, S. Piligkos, *Angew. Chem. Int. Ed.* **2002**, *41*, 4318–4321; e) C. P. Paptopoulou, V. Tangoulis, E. Devlin, *Angew. Chem. Int. Ed.* **2002**, *41*, 2386–2389; f) R. W. Saalfrank, I. Bernt, M. M. Chowdhry, F. Hampel, G. B. M. Vaughan, *Chem. Eur. J.* **2001**, *7*, 2765–2769.

[9] A selection of recent articles: a) A. V. Postnikov, J. Kortus, M. R. Pederson, *Phys. Status Solidi B* **2006**, *243*, 2533–2572 and literature cited therein; b) E. Ruiz, S. Alvarez, *ChemPhysChem* **2005**, *6*, 1094–1099; c) A. V. Postnikov, J. Kortus, S. Bluegel, *Mol. Phys. Rep.* **2003**, *38*, 56–63; d) I. Rudra, S. Ramasesha, D. Sen, *Phys. Rev. B* **2002**, *66*, 014441/1–014441/9.

[10] a) O. L. Sydora, T. P. Henry, P. T. Wolczanski, E. B. Lobkovsky, E. Rumberger, D. N. Hendrickson, *Inorg. Chem.* **2006**, *45*, 609–626; b) O. L. Sydora, P. T. Wolczanski, E. B. Lobkovsky, *Angew. Chem. Int. Ed.* **2003**, *42*, 2685–2687.

[11] G. Mezei, C. M. Zaleski, V. L. Pecoraro, *Chem. Rev.* **2007**, *107*, 4933–5003.

[12] a) L. Cheng, W.-X. Zhang, B.-H. Ye, J.-B. Lin, X.-M. Chen, *Inorg. Chem.* **2007**, *46*, 1135–1143; b) H. Link, P. Reiss, S. Chitsaz, H. Pfistner, D. Fenske, *Z. Anorg. Allg. Chem.* **2003**, *629*, 755–768; c) C. S. Alvarez, A. Bashall, A. D. Bond, D. Cave, E. A. Harron, R. A. Layfield, M. E. G. Mosquera, M. McPartlin, J. M. Rawson, P. T. Wood, D. S. Wright, *Dalton Trans.* **2003**, 3002–3008; d) C. S. Alvarez, A. D. Bond, E. A. Harron, R. A. Layfield, J. A. McAllister, C. M. Pask, J. M. Rawson, D. S. Wright, *Organometallics* **2001**, *20*, 4135–4137; e) W. J. Grigsby, P. P. Power, *J. Chem. Soc., Dalton Trans.* **1996**, 4613–4615.

[13] See for example, a) T. Stamatatos, K. A. Abboud, W. Wernsdorfer, G. Christou, *Angew. Chem. Int. Ed.* **2007**, *46*, 884–888; b) T. Stamatatos, K. A. Abboud, W. Wernsdorfer, G. Christou, *Angew. Chem. Int. Ed.* **2006**, *45*, 4134–4137.

[14] M. Ostermeier, C. Limberg, B. Ziemer, V. Karunakaran, *Angew. Chem. Int. Ed.* **2007**, *46*, 5329–5331.

[15] N. Y. M. Iha, M. A. de Almeida Azzelini, S. Utsuno, *Polyhedron* **1998**, *17*, 3379–3390.

[16] K. Ogura, Y. Kurasawa, Y. Yamaguchi, Y. Okamoto, *Heterocycles* **2003**, *59*, 283–291.

[17] A. Murso, D. Stalke, *Eur. J. Inorg. Chem.* **2004**, 4272–4277.

[18] A. Murso, D. Stalke, *Dalton Trans.* **2004**, 2563–2569.

[19] H. Grützmacher, *Angew. Chem. Int. Ed.* **2008**, *47*, 1814–1818.

[20] M. Westerhausen, T. Bollwein, N. Makropoulos, T. M. Rotter, T. Habereder, M. Suter, H. Nöth, *Eur. J. Inorg. Chem.* **2001**, 851–857.

[21] M. Westerhausen, T. Bollwein, N. Makropoulos, S. Schneiderbauer, M. Suter, H. Nöth, P. Mayer, H. Piotrowski, K. Polborn, A. Pfitzner, *Eur. J. Inorg. Chem.* **2002**, 389–404.

[22] a) A. E. Clark, E. R. Davidson, *J. Chem. Phys.* **2001**, *115*, 7382–7392; b) C. Herrmann, M. Reiher, B. A. Hess, *J. Chem. Phys.* **2005**, *122*, 034102.

[23] a) I. Mayer, *Chem. Phys. Lett.* **2007**, *440*, 357–359; b) M. Podewitz, C. Herrmann, A. Malassa, M. Westerhausen, M. Reiher, *Chem. Phys. Lett.* **2008**, *451*, 301–308.

[24] C. Herrmann, L. Yu, M. Reiher, *J. Comput. Chem.* **2006**, *27*, 1223–1239.

[25] D. C. Bradley, M. B. Hursthouse, C. W. Newing, A. J. Welch, *J. Chem. Soc., Chem. Commun.* **1972**, 567–568.

[26] K. H. D. Ballem, V. Shetty, N. Etkin, B. O. Patrick, K. M. Smith, *Dalton Trans.* **2004**, 3431–3433.

[27] D. C. Bradley, M. B. Hursthouse, A. A. Ibrahim, K. M. Abdul Malik, M. Motevalli, R. Möseler, H. Powell, J. D. Runnacles, A. C. Sullivan, *Polyhedron* **1990**, *9*, 2959–2964.

[28] M. M. Olmstead, P. P. Power, S. C. Shoner, *Inorg. Chem.* **1991**, *30*, 2547–2551.

[29] R. A. Andersen, K. Faegri, J. C. Green, A. Haaland, M. F. Lappert, W.-P. Leung, K. Rypdal, *Inorg. Chem.* **1988**, *27*, 1782–1786.

[30] D. C. Bradley, M. B. Hursthouse, K. M. Abdul Malik, R. Möseler, *Transition Met. Chem.* **1978**, *3*, 253–254.

[31] B. D. Murray, P. P. Power, *Inorg. Chem.* **1984**, *23*, 4584–4588.

[32] I. van Meervelt, M. Goethals, N. Leroux, T. Zeegers-Huyskens, *J. Phys. Org. Chem.* **1997**, *10*, 680–686.

[33] a) M. Reiher, *J. Chem. Soc. Faraday Trans.* **2007**, *135*, 97–124; b) M. Reiher, *Inorg. Chem.* **2002**, *41*, 6928–6935; c) O. Salomon, M. Reiher, B. A. Hess, *J. Chem. Phys.* **2002**, *117*, 4729–4737; d) M. Reiher, O. Salomon, B. A. Hess, *Theor. Chem. Acc.* **2001**, *107*, 48–55.

[34] L. Noodleman, T. Lovell, W.-G. Han, J. Li, F. Himo, *Chem. Rev.* **2004**, *104*, 459–508.

[35] C. Herrmann, M. Podewitz, M. Reiher, *Int. J. Quantum Chem.* **2009**, *109*, 2430–2446.

[36] R. Ahlrichs, M. Bär, M. Häser, H. Horn, C. Kömel, *Chem. Phys. Lett.* **1989**, *162*, 165–169.

[37] a) A. D. Becke, *Phys. Rev. A* **1988**, *38*, 3098–3100; b) J. P. Perdew, *Phys. Rev. B* **1986**, *33*, 8822–8824.

[38] a) A. D. Becke, *J. Chem. Phys.* **1993**, *98*, 5648–5652; b) C. Lee, W. Yang, R. G. Parr, *Phys. Rev. B* **1988**, *37*, 785–789.

[39] a) A. Schäfer, C. Huber, R. Ahlrichs, *J. Chem. Phys.* **1994**, *100*, 5829–5835; b) A. Schäfer, H. Horn, R. Ahlrichs, *J. Chem. Phys.* **1992**, *97*, 2571–2577.

[40] *COLLECT*, Data Collection Software, Nonius B. V., Netherlands, **1998**.

[41] Z. Otwinowski, W. Minor, "Processing of X-ray Diffraction Data Collected in Oscillation Mode" in *Methods in Enzymology, Vol. 276, Macromolecular Crystallography, Part A* (Ed.: C. W. Carter & R. M. Sweet), Academic Press San Diego, **1997**, pp. 307–326.

[42] SORTAV, R. H. Blessing, *Acta Crystallogr., Sect. A* **1995**, *51*, 33–38.

[43] G. M. Sheldrick, *Acta Crystallogr., Sect. A* **1990**, *46*, 467–473.

[44] G. M. Sheldrick, *SHELXL-97 (Release 97–2)*, University of Göttingen, Germany, **1997**.

Received: November 30, 2009